

BANMo: Building Animatable 3D Neural Models from Many Casual Videos

Gengshan Yang^{2*} Minh Vo³ Natalia Neverova¹ Deva Ramanan² Andrea Vedaldi¹ Hanbyul Joo¹
¹Meta AI ²Carnegie Mellon University ³Meta Reality Labs

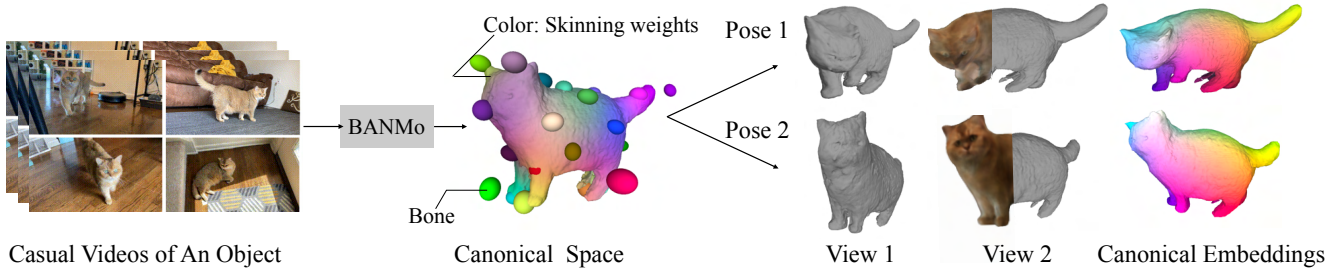


Figure 1. Given multiple casual videos capturing a deformable object, BANMo reconstructs an animatable 3D model, including an implicit canonical 3D shape, appearance, skinning weights, and time-varying articulations, without pre-defined shape templates or registered cameras. **Left:** Input videos; **Middle:** 3D shape, bones, and skinning weights (visualized as surface colors) in the canonical space; **Right:** Posed reconstruction at each time instance with color and canonical embeddings (correspondences are shown as the same colors).

Abstract

Prior work for articulated 3D shape reconstruction often relies on specialized multi-view and depth sensors or pre-built deformable 3D models. Such methods do not scale to diverse sets of objects in the wild. We present a method that requires neither of them. It aims to create high-fidelity, articulated 3D models from many casual RGB videos in a differentiable rendering framework. Our key insight is to merge three schools of thought: (1) classic deformable shape models that make use of articulated bones and blend skinning, (2) canonical embeddings that establish correspondences between pixels and a canonical 3D model, and (3) volumetric neural radiance fields (NeRFs) that are amenable to gradient-based optimization. We introduce neural blend skinning models that allow for differentiable and invertible articulated deformations. When combined with canonical embeddings, such models allow us to establish dense correspondences across videos that can be self-supervised with cycle consistency. On real and synthetic datasets, our method shows higher-fidelity 3D reconstructions than prior works for humans and animals, with the ability to render realistic images from novel viewpoints. Project page: <https://banmo-www.github.io/>.

1. Introduction

We are interested in developing tools that can reconstruct accurate and animatable models of 3D objects from casually collected videos. A representative application is content creation for virtual and augmented reality, where the goal is to 3D-ify images and videos captured by users for consumption in a 3D space or creating animatable assets such as avatars. For rigid scenes, traditional Structure from Motion (SfM) approaches can be used to leverage large collection of uncontrolled images, such as images downloaded from the web, to build accurate 3D models of landmarks and entire cities [1, 45, 46]. However, these approaches do not generalize to deformable objects such as family members, friends or pets, which are often the focus of user content.

We are thus interested in reconstructing 3D deformable objects from *casually collected videos*. However, individual videos may not contain sufficient information to obtain good reconstruction of a given subject. Fortunately, we can expect that users may collect several videos of the same subjects, such as filming a family member or a pet over the span of several months or years. In this case, we wish our system to gather information from *all available videos* into a single 3D model, bridging any time discontinuity.

In this paper, we present **BANMo**, a **B**uilder of **A**nimatable 3D **N**eural **M**odels from multiple casual RGB videos. By consolidating the 2D cues from thousands of images into a fixed canonical space, BANMo learns a high-

*Work done when interning at Meta AI

fidelity neural implicit model for appearance, 3D shape, and articulations of the target non-rigid object. The articulation of the output model of BANMo is expressed by a neural blend skinning model, similar to [5, 39, 64, 65], making the output *animatable* by manipulating bone transformations.

As shown in NRSfM [4], reconstructing a freely moving non-rigid object from monocular video is challenging, where epipolar constraints are not directly applicable. We address three core challenges in BANMo: (1) how to represent 3D geometry and appearance of the target in a canonical space; (2) how to deform 3D points between canonical space and individual time instances; (3) how to find pixel or part correspondences over videos given different viewpoint, lighting, background, and object deformations.

Concretely, we utilize neural implicit functions [29] to represent color and 3D surface in the canonical space. This representation enables higher-fidelity 3D geometry reconstruction compared to approaches based on 3D meshes [64, 65]. The use of neural blending skinning in BANMo provides a way to constrain the deformation space of the target object, allowing better handling of pose variations and deformations with unknown camera parameters, compared to dynamic NeRF approaches [5, 22, 33, 38]. To find correspondences, we present a module that performs dense matching between pixels and an implicit feature volume. Finally, for robust and efficient optimization over a large number of video frames, we pre-train a pose network for human and quadruped animals to provide initial camera orientations. In a nutshell, BANMo presents a way to merge the recent non-rigid object reconstruction approaches [64, 65] in a dynamic NeRF framework [5, 22, 33, 38], to achieve higher-fidelity non-rigid object reconstruction. We show experimentally that BANMo produces higher-fidelity 3D shape details than previous state-of-the-art approaches [65], by taking better advantage of the large number of frames in multiple videos.

2. Related work

Human and animal body models. A large body of work in 3D human and animal reconstruction uses parametric shape models [25, 35, 56, 61, 72, 73], which are built from registered 3D scans of human or animals, and serve to recover 3D shapes given a single image or video at test time [2, 3, 15, 15, 71]. Although parametric body models achieve great success in reconstructing human with large amounts of ground-truth 3D data, it is challenging to apply the same methodology to categories with limited 3D data, such as animals and humans in diverse sets of clothing.

Category reconstruction from images or videos. A number of recent methods build deformable 3D models of object categories from images or videos with weak 2D annotations, such as keypoints, object silhouettes, and optical flow, obtained from human annotators or predicted by off-the-shelf models [7, 12, 16, 20, 21, 60, 68]. Such methods

often rely on a coarse shape template [18, 54, 70], and are not able to recover fine-grained details or large deformations. Recently, HDNet [10] uses social media videos to learn depth estimators for clothed human.

Category-agnostic video shape reconstruction. Non-rigid structure from motion (NRSfM) methods [4, 8, 17, 19, 43] reconstruct non-rigid 3D shapes from a set of 2D point trajectories in a class-agnostic way. However, due to difficulties in obtaining accurate long-range correspondences [40, 49], they do not work well for videos in the wild. Recent efforts such as LASR and ViSER [64, 65] reconstruct articulated shapes from a monocular video with differentiable rendering. As our results show, they may still produce blurry geometry and unrealistic articulations.

Neural radiance fields. Prior works on NeRF optimize a continuous scene function for novel view synthesis given a set of images, often assuming the scene is rigid and camera poses can be accurately registered to the background [11, 23, 27–29, 59]. To extend NeRF to dynamic scenes, recent works introduce additional functions to deform observed points to a canonical space or over time [22, 33, 34, 38, 53, 57]. However, they heavily rely on background registration, and fail when the motion between objects and background is large. Moreover, the deformations cannot be explicitly controlled by user inputs. Similar to our goal, some recent works [24, 32, 36, 37, 47] produce pose-controllable NeRFs, but they rely on a human body model, or synchronized multi-view video inputs.

3. Method

We model the deformable object in a canonical time-invariant space, i.e. the *rest* body pose space, that can be transformed to the *articulated* pose in the camera space at each time instance with forward mappings, and transform back with backward mappings. We use implicit functions to represent the 3D shape, color, and dense semantic embeddings of the object. Our neural 3D model can be deformed and rendered into images at each time instance via differentiable volume rendering, and optimized to ensure consistency between the rendered images and multiple cues in the observed images, including color, silhouette, optical flow, and pixel feature embeddings. We refer readers to the overview in Fig. 2 and the list of notations in supplement.

3.1. Shape, Appearance, and Warping Model

We first represent shape and appearance of deformable objects in a canonical time-invariant *rest pose* space.

Canonical shape model. In order to model the shape and appearance of an object in a canonical space, we use a method inspired by Neural Radiance Fields (NeRF) [29]. A 3D point $\mathbf{X}^* \in \mathbb{R}^3$ in the canonical space is associated with three properties: color $\mathbf{c} \in \mathbb{R}^3$, density $\sigma \in [0, 1]$, and

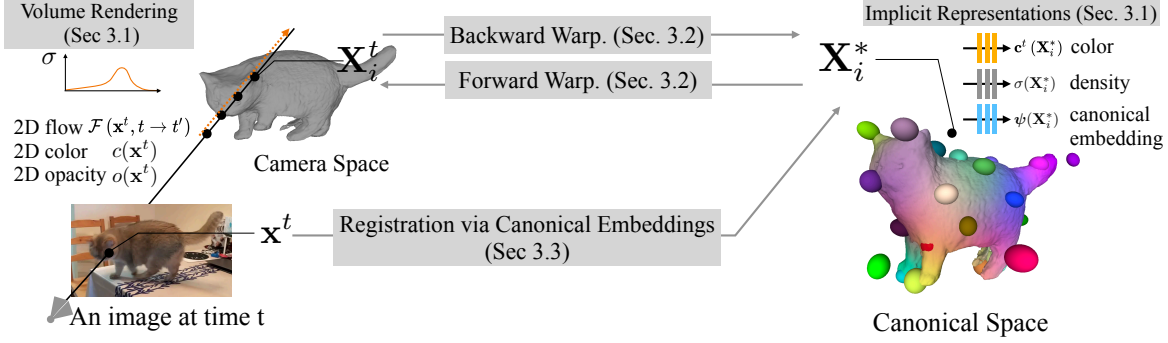


Figure 2. **Method overview.** BANMo optimizes a set of shape and deformation parameters (Sec. 3.1) that describe the video observations in pixel colors, silhouettes, optical flow, and higher-order features descriptors, based on a differentiable volume rendering framework. BANMo uses a neural blend skinning model (Sec. 3.2) to transform 3D points between the camera space and the canonical space, enabling handling large deformations. To register pixels across videos, BANMo jointly optimizes an implicit canonical embedding (CE) (Sec. 3.3).

a canonical embedding $\psi \in \mathbb{R}^{16}$. These properties are predicted by the Multilayer Perceptron (MLP) networks:

$$\mathbf{c}^t = \text{MLP}_{\mathbf{c}}(\mathbf{X}^*, \mathbf{v}^t, \omega_e^t), \quad (1)$$

$$\sigma = \Gamma_{\beta}(\text{MLP}_{\text{SDF}}(\mathbf{X}^*)), \quad (2)$$

$$\psi = \text{MLP}_{\psi}(\mathbf{X}^*). \quad (3)$$

As in NeRF, color \mathbf{c}^t also depends on a time-varying view direction $\mathbf{v}^t \in \mathbb{R}^2$ and a learnable environment code $\omega_e^t \in \mathbb{R}^{64}$ that captures environment illumination conditions [27].

The shape is given by MLP_{SDF} , computing the Signed-Distance Function (SDF) of a point to the surface. To convert SDF to density σ for volume rendering, we use the cumulative of a unimodal distribution with zero mean and β scale, denoted as $\Gamma_{\beta}(x)$. β is a learnable parameter that controls the solidness of the object, approaching zero for solid objects [58, 66]. Prior works [58, 66] have explored the cumulative of Logistic and Laplace distribution respectively and we follow VolSDF [66] to use the accumulative of Laplace distribution. Compared with ReLU or Softplus activations used in NeRF, it provides a principled way of extracting surface as the zero level-set of the SDF.

Finally, the MLP_{ψ} network maps 3D points to a canonical feature embedding ψ that can be matched by pixels from different viewpoints and lighting conditions, enabling long-range correspondence across videos. This feature can be interpreted as a variant of Continuous Surface Embeddings (CSE) [30] but defined volumetrically.

Space-time warping model. We consider a pair of time-dependent warping functions: *forward warping function* $\mathcal{W}^{t, \rightarrow} : \mathbf{X}^* \rightarrow \mathbf{X}^t$ mapping canonical location \mathbf{X}^* to camera space location \mathbf{X}^t at current time and the *backward warping function* $\mathcal{W}^{t, \leftarrow} : \mathbf{X}^t \rightarrow \mathbf{X}^*$ for inverse mapping.

Prior work such as Nerfies [33] and Neural Scene Flow Fields (NSFF) [22] learn deformations under the assumptions of known camera poses and small object deformation. As detailed in Sec. 3.2 and Sec. 3.4, we do not

make such assumptions; instead, we adopt a neural blend-skinning model that can handle large deformations without a pre-defined skeleton model.

Volume rendering. To render images, we use volume rendering in NeRF [29], but warp the 3D ray to account for deformation [33]. Specifically, let $\mathbf{x}^t \in \mathbb{R}^2$ be the pixel location at time t , and $\mathbf{X}_i^t \in \mathbb{R}^3$ be the i -th 3D point sampled along the ray emanates from \mathbf{x}^t . As the color and density are defined in the canonical space, we *pull back* the sampled points to the canonical space using $\mathbf{X}_i^* = \mathcal{W}^{t, \leftarrow}(\mathbf{X}_i^t)$. The color \mathbf{c} and the opacity $o \in [0, 1]$ are then given by:

$$\mathbf{c}(\mathbf{x}^t) = \sum_{i=1}^N \tau_i \mathbf{c}_i^t, \quad o(\mathbf{x}^t) = \sum_{i=1}^N \tau_i, \quad (4)$$

where N is the number of samples and τ_i is the free-flight probability that a photon travels between the camera center and the i -th sample, as given by $\tau_i = \prod_{j=1}^{i-1} p_j (1 - p_j)$. Here $p_i = \exp(-\sigma_i \delta_i)$ is the probability that the photon is transmitted through the interval δ_i between the i -th sample and the next. Color \mathbf{c}_i and density σ_i are computed by Eq. 1-2. We further compute the expected surface intersection:

$$\mathbf{X}^*(\mathbf{x}^t) = \sum_{i=1}^N \tau_i \mathbf{X}_i^*. \quad (5)$$

To render 2D flow, we *push forward* the warped ray points to another time t' via forward warping $\mathcal{W}^{t', \rightarrow}$ to find its expected 2D re-projection:

$$\mathbf{x}^{t'} = \sum_{i=1}^N \tau_i \Pi^{t'} \left(\mathcal{W}^{t', \rightarrow}(\mathbf{X}_i^*) \right), \quad (6)$$

where $\Pi^{t'}$ is the projection matrix of a pinhole camera. We optimize video-specific $\Pi^{t'}$ given a rough initialization. With this, we compute a 2D flow rendering as:

$$\mathcal{F}(\mathbf{x}^t, t \rightarrow t') = \mathbf{x}^{t'} - \mathbf{x}^t. \quad (7)$$

3.2. Deformation Model via Neural Blend Skinning

We define mappings $\mathcal{W}^{t,\rightarrow}$ and $\mathcal{W}^{t,\leftarrow}$ based on a neural blend skinning model approximating articulated body motion. Defining invertible warps for neural deformation representations is difficult [5]. Our formulation represents 3D warps as compositions of neural-weighted *rigid-body transformations*, each of which is differentiable and invertible.

Blend skinning deformation. Given a 3D point \mathbf{X}^t at time t , we wish to find its corresponding 3D point \mathbf{X}^* in the canonical space. Conceptually, \mathbf{X}^* can be considered as points in the *rest* pose at a fixed camera view point. Our formulation finds mappings between \mathbf{X}^t and \mathbf{X}^* by blending the rigid transformations of 3D coordinate of bones. Let $\mathbf{G}^t \in SE(3)$ be a transformation of the object root body from canonical space to time t , and $\mathbf{J}_b^t \in SE(3)$ be a rigid transformation that moves the b -th bone from its rest configuration to deformed state t , then we have

$$\mathbf{X}^t = \mathcal{W}^{t,\rightarrow}(\mathbf{X}^*) = \mathbf{G}^t \mathbf{J}^{t,\rightarrow} \mathbf{X}^*, \quad (8)$$

$$\mathbf{X}^* = \mathcal{W}^{t,\leftarrow}(\mathbf{X}^t) = \mathbf{J}^{t,\leftarrow} (\mathbf{G}^t)^{-1} \mathbf{X}^t, \quad (9)$$

where $\mathbf{J}^{t,\rightarrow}$ and $\mathbf{J}^{t,\leftarrow}$ are weighted averages of B rigid transformations $\{\mathbf{J}_b^t\}_{b \in \{1, \dots, B\}}$ that move the bones between rest configurations and time t configurations. Following linear blend skinning deformation [9], we have

$$\mathbf{J}^{t,\rightarrow} = \sum_{b=1}^B \mathbf{W}_b^{t,\rightarrow} \mathbf{J}_b^t, \quad \mathbf{J}^{t,\leftarrow} = \sum_{b=1}^B \mathbf{W}_b^{t,\leftarrow} (\mathbf{J}_b^t)^{-1}, \quad (10)$$

where $\mathbf{W}_b^{t,\rightarrow}$ and $\mathbf{W}_b^{t,\leftarrow}$ represent pose-dependent skinning weights that assigns point \mathbf{X}^* and \mathbf{X}^t to the b -th bone.

Pose representation. We represent poses with angle-axis rotations and 3D translations, regressed from MLPs:

$$\mathbf{G}^t = \text{MLP}_{\mathbf{G}}(\omega_r^t), \quad \mathbf{J}_b^t = \text{MLP}_{\mathbf{J}}(\omega_b^t) \quad (11)$$

where ω_r^t and ω_b^t are 128-dimensional latent codes for root pose and body pose at frame t respectively. Compared with directly optimizing $SE(3)$ poses, we find such over-parameterized representations converges better with stochastic first-order gradient methods. Instead of treating pose codes as independent parameters learned per-frame, we represent each dimension of the latent code as linear combinations of sinusoidal basis functions:

$$\omega_i^b = \mathbf{A}_i \mathcal{F}(t) \quad (12)$$

where $\mathcal{F}(\cdot)$ is a 1D basis of sines and cosines with linearly-increasing frequencies at log-scale [50], and we learn separate weight matrices $\mathbf{A}_{i \in \{1, \dots, M\}}$ for each video. The frame index t is normalized by the maximum video length $\max_{i=1}^M |T_i|$. Using the temporal Fourier basis stabilizes the optimization and produces more smooth deformations.

Skinning weights. Similar to SCANimate [39], we define a skinning weight function $\mathcal{S} : (\mathbf{X}, \omega_b) \rightarrow \mathbf{W} \in \mathbb{R}^B$ that assigns \mathbf{X} to bones given body pose code ω_b . During backward mapping, we apply \mathcal{S} to time t points and pose codes ω_b^t to compute backward skinning weights $\mathbf{W}^{t,\leftarrow}$. During forward mapping, we apply the same \mathcal{S} to the canonical space points and rest pose code ω_b^* to compute the forward skinning weights $\mathbf{W}^{t,\rightarrow}$.

Directly representing \mathcal{S} as neural networks can be difficult to optimize. Therefore, we condition neural skinning weights on explicit 3D Gaussian ellipsoids that move along with the bone coordinates. Similar to LASR [64], the Gaussian skinning weights are determined by the Mahalanobis distance between \mathbf{X} and the Gaussian ellipsoids:

$$\mathbf{W}_\sigma = (\mathbf{X} - \mathbf{C}_b)^T \mathbf{Q}_b (\mathbf{X} - \mathbf{C}_b), \quad (13)$$

where $\mathbf{C}_b \in \mathbb{R}^{B \times 3}$ are bone centers and $\mathbf{Q}_b = \mathbf{V}_b^T \mathbf{\Lambda}_b^0 \mathbf{V}_b$ are the precision matrices composed by bone orientations $\mathbf{V}_b \in \mathbb{R}^{B \times 3 \times 3}$ and diagonal scale matrices $\mathbf{\Lambda}_b^0 \in \mathbb{R}^{B \times 3 \times 3}$. When computing backward skinning weights, bone centers and orientations are transformed as $(\mathbf{V}_b | \mathbf{C}_b) = \mathbf{J}_b (\mathbf{V}_b^0 | \mathbf{C}_b^0)$, where \mathbf{J}_b are bone transforms in Eq. 11. $\mathbf{\Lambda}_b^0$, \mathbf{V}_b^0 and \mathbf{C}_b^0 are learnable rest bone configurations.

To model the skinning weights for fine geometry, we find it helpful to add delta skinning weights after the coarse component is well-optimized. Delta skinning weights are represented as a coordinated-MLP, $\mathbf{W}_\Delta = \text{MLP}_\Delta(\mathbf{X}, \omega_b) \in \mathbb{R}^B$. The final skinning function is the sum of the coarse and fine components, normalized by a softmax function,

$$\mathbf{W} = \mathcal{S}(\mathbf{X}, \omega_b) = \sigma_{\text{softmax}}(\mathbf{W}_\sigma + \mathbf{W}_\Delta). \quad (14)$$

The Gaussian component regularizes the skinning weights to be spatially smooth and temporally consistent, and handles large deformations better than purely implicitly-defined ones. Furthermore, our formulation of the skinning weights are dependent on only pose status by construction, and therefore regularizes the space of skinning weights.

3.3. Registration via Canonical Embeddings

To register pixel observations at different time instances, BANMo maintains a canonical feature embedding that encodes semantic information of 3D points in the canonical space, which can be uniquely matched by the pixel features, and provide strong cues for registration via a joint optimization of shape, articulations, and embeddings.

Canonical embeddings matching. Given a pixel at \mathbf{x}^t of frame t , our goal is to find a point \mathbf{X}^* in the canonical space whose feature embedding $\psi(\mathbf{X}^*) \in \mathbb{R}^{16}$ best matches the pixel feature embedding $\psi_I^t(\mathbf{x}^t) \in \mathbb{R}^{16}$. The pixel embeddings ψ_I^t (of frame t) are computed by a CNN. Different from ViSER [65] that learns embeddings from scratch, we initialize pixel embeddings with CSE [30, 31] that produces

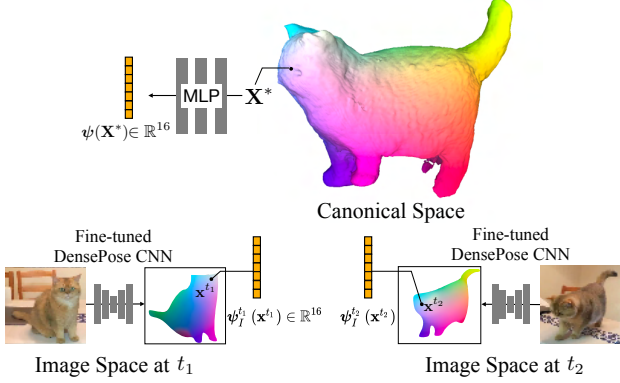


Figure 3. **Canonical Embeddings.** We jointly optimize an implicit function to produce canonical embeddings from 3D canonical points that match to the 2D DensePose CSE embeddings [30].

consistent features for semantically corresponding pixels, and optimize pixel and canonical embeddings jointly. Recall that the embedding of a canonical 3D point is computed as $\psi(\mathbf{X}^*) = \text{MLP}_\psi(\mathbf{X}^*)$ in Eq. 3. Intuitively, MLP_ψ is optimized to ensure the output 3D descriptor matches 2D descriptors of corresponding pixels across multiple views. To compute the 3D surface point corresponding to a 2D point \mathbf{x}^t , we apply soft argmax descriptor matching [13,26]:

$$\hat{\mathbf{X}}^*(\mathbf{x}^t) = \sum_{\mathbf{X} \in \mathbf{V}^*} \tilde{s}^t(\mathbf{x}^t) \mathbf{X}, \quad (15)$$

where \mathbf{V}^* are sampled points in a tightly-bounded canonical 3D grid, and \tilde{s} is a normalized distribution of feature matches over the 3D grid: $\tilde{s}^t(\mathbf{x}^t) = \sigma_{\text{softmax}}(\alpha_s \langle \psi_I^t(\mathbf{x}^t), \psi(\mathbf{X}) \rangle)$, where α_s is a learnable scaling to control the peakness of the softmax function and $\langle \cdot, \cdot \rangle$ is the cosine similarity.

Self-supervised canonical embedding learning. As describe later in Eq. 17-18, the canonical embedding is self-supervised by enforcing the consistency between feature matching and geometric warping. By jointly optimizing the shape and articulation parameters via consistency losses, canonical embeddings provide strong cues to register pixels from different time instance to the canonical 3D space, and enforce a coherent reconstruction given observations from multiple videos, as validated in ablation studies (Sec. 4.3).

3.4. Optimization

Given multiple videos, we optimize all parameters described above, including MLPs, $\{\text{MLP}_e, \text{MLP}_{\text{SDF}}, \text{MLP}_\psi, \text{MLP}_G, \text{MLP}_J, \text{MLP}_\Delta\}$, learnable codes $\{\omega_e^t, \omega_r^t, \omega_b^t, \omega_b^*\}$ and pixel embeddings ψ_I .

Losses. The model is learned by minimizing three types of losses: reconstruction losses, geometric feature registration

losses, and a 3D cycle-consistency regularization loss:

$$\mathcal{L} = \underbrace{(\mathcal{L}_{\text{sil}} + \mathcal{L}_{\text{rgb}} + \mathcal{L}_{\text{OF}})}_{\text{reconstruction losses}} + \underbrace{(\mathcal{L}_{\text{match}} + \mathcal{L}_{2\text{D-cyc}})}_{\text{feature registration losses}} + \mathcal{L}_{3\text{D-cyc}}.$$

Reconstruction losses are similar to those in existing differentiable rendering pipelines [29,67]. Besides color loss \mathcal{L}_{rgb} and silhouette loss \mathcal{L}_{sil} , we further compute flow reconstruction losses \mathcal{L}_{OF} by comparing the rendered \mathcal{F} defined in Eq. 7 with the observed 2D optical flow $\hat{\mathcal{F}}$ computed by an off-the-shelf flow network:

$$\mathcal{L}_{\text{rgb}} = \sum_{\mathbf{x}^t} \|\mathbf{c}(\mathbf{x}^t) - \hat{\mathbf{c}}(\mathbf{x}^t)\|^2, \quad \mathcal{L}_{\text{sil}} = \sum_{\mathbf{x}^t} \|\mathbf{o}(\mathbf{x}^t) - \hat{\mathbf{s}}(\mathbf{x}^t)\|^2,$$

$$\mathcal{L}_{\text{OF}} = \sum_{\mathbf{x}^t, (t, t')} \left\| \mathcal{F}(\mathbf{x}^t, t \rightarrow t') - \hat{\mathcal{F}}(\mathbf{x}^t, t \rightarrow t') \right\|^2, \quad (16)$$

where $\hat{\mathbf{c}}$ and $\hat{\mathbf{s}}$ are observed color and silhouette. Additionally, we define feature matching losses to enforce 3D points predicted via canonical embedding $\hat{\mathbf{X}}^*(\mathbf{x}^t)$ (Eq. 15) to match the prediction from backward warping (Eq. 5):

$$\mathcal{L}_{\text{match}} = \sum_{\mathbf{x}^t} \left\| \hat{\mathbf{X}}^*(\mathbf{x}^t) - \mathbf{X}^*(\mathbf{x}^t) \right\|_2^2, \quad (17)$$

and a geometric cycle consistency loss [18,65] that forces the image projection after forward warping of $\hat{\mathbf{X}}^*(\mathbf{x}^t)$ to land back on its original 2D coordinates:

$$\mathcal{L}_{2\text{D-cyc}} = \sum_{\mathbf{x}^t} \left\| \Pi^t \left(\mathcal{W}^{t, \rightarrow}(\hat{\mathbf{X}}^*(\mathbf{x}^t)) \right) - \mathbf{x}^t \right\|_2^2. \quad (18)$$

Similar to NSFF [22], we regularize the deformation function $\mathcal{W}^{t, \rightarrow}(\cdot)$ and $\mathcal{W}^{t, \leftarrow}(\cdot)$ by a 3D cycle consistency loss, which encourages a sampled 3D point in the camera coordinates to be backward deformed to the canonical space and forward deformed to its original location:

$$\mathcal{L}_{3\text{D-cyc}} = \sum_i \tau_i \left\| \mathcal{W}^{t, \rightarrow} \left(\mathcal{W}^{t, \leftarrow}(\mathbf{X}_i^t) \right) - \mathbf{X}_i^t \right\|_2^2, \quad (19)$$

where τ_i is the opacity that weighs the sampled points so that a point near the surface receives heavier regularization.

Our optimization is highly non-linear with local minima. To improve the robustness of optimization, we consider the following initialization strategy for root body poses.

Root pose initialization. We provide a rough per-frame initialization of root poses (\mathbf{G}^t in Eq. 8), similar to NeRS [69]. Specifically, we train a separate network PoseNet, which is applied to every test video frame. Similar to DenseRaC [62], PoseNet takes a DensePose CSE [30] feature image as input and predicts the root pose $\mathbf{G}_0^t = \text{PoseNet}(\psi_I^t)$, where

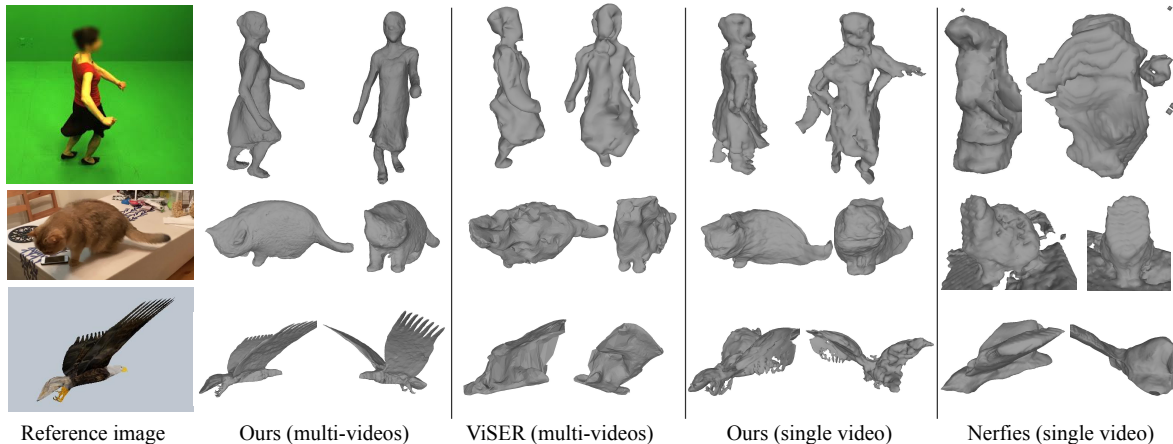


Figure 4. **Qualitative comparison of our method with prior art [33,65].** From top to bottom: AMA’s samba, casual-cat, eagle.

$\psi_I^t \in \mathbb{R}^{112 \times 112 \times 16}$ is the embedding output of DensePose CSE [30] from an RGB image I_t . We train PoseNet by a synthetic dataset produced offline. See supplement for details on training. Given the pre-computed G_0^t , BANMo only needs to compute a delta root pose via MLP:

$$G^t = \text{MLP}_G(\omega_r^t)G_0^t. \quad (20)$$

4. Experiments

Implementation details. Our implementation of implicit shape and appearance models follows NeRF [29], except that our shape model outputs SDF, which is transformed to density for volume rendering. To extract the rest surface, we find the zero-level set of SDF by running marching cubes on a 256^3 grid. To obtain articulated shapes at each time instance, we articulate points on the rest surface with forward deformation $\mathcal{W}^{t, \rightarrow}$.

Optimization details. We initialize MLP_{SDF} such that it approximates a unit sphere [67]. We use $B = 25$ rest bones, which are initialized with unit scale, identity orientation, and centers uniformly spaced on the initial rest surface. During optimization, we reinitialize the rest bones at $\{20\%, 67\%$ of total iterations and further encourage them to stay close to the surface with a Sinkhorn divergence loss [6]. In a batch, we sample $N^I = 512$ image pairs and sample $N^P = 6144$ pixels from all image pairs for rendering. The interval between image pairs is randomly chosen $\Delta T \in \{1, 2, 4, 8, 16, 32\}$. To stabilize optimization, we observe that N_I needs to roughly match the number of input frames. The reconstruction quality improves with more iterations and we find 36k iterations (15 hours on a V100 GPU) already produces high-fidelity details. Please find a list of hyper-parameters in supplement.

4.1. Dataset and Metrics

Qualitative: Casual videos dataset. We demonstrate BANMo’s ability to reconstruct 3D models from casual videos of animals and humans. Object silhouette and optical flow (for computing reconstruction losses Eq. 16) are extracted by off-the-shelf models, PointRender and VCN-robust [14,63]. Two special challenges arise from the casual nature of the video captures. First, each video collection contains around 1k images, an order of magnitudes larger those used in prior work [22,29,33,65], which requires the method to handle reconstructions at a larger scale. Second, the dataset makes no control over camera movement or object movement. In particular, objects freely moves in a video and background changes across videos, posing challenges to standard SfM pipelines to estimate the object root poses. We show results on 11 videos (totaling 900 images) of a British shorthair cat denoted as `casual-cat` below. Please find other results in the project webpage.

Quantitative: AMA human dataset. Articulated Mesh Animation (AMA) dataset [55] contains multi-view videos captured by 8 synchronized cameras. It provides high-fidelity ground-truth meshes with clothing. We use 2 sets of videos of the same actor (swing and samba), totaling 2600 frames, as the input to optimization. We use the ground-truth object silhouettes. Time synchronization and camera extrinsics are *not* used.

Quantitative: Animated Objects dataset. We download free animated 3D models from TurboSquid, including an eagle model and a model for human hands. We render them from different camera trajectories with partially overlapping motions. Each animated object is rendered as 5 videos with 150 frames per video. We provide ground-truth root poses and object silhouettes to BANMo and baselines.

Metrics. We quantify the results using both Chamfer dis-

Table 1. **Quantitative results on AMA and Animated Objects.** 3D Chamfer distance (cm, \downarrow) and F-score (% , \uparrow) averaged over all frames. The 3D models for *eagle* and *hands* are resized such that the longest edge of the axis-aligned object bounding box is 2m. * *with ground-truth root poses*. *S*: single-video results. All methods are assigned with the same initial root pose.

Method	AMA-swing		Eagle*		Hands*	
	CD	F@2%	CD	F@2%	CD	F@2%
Ours	9.1	57.0	8.1	56.7	7.5	49.6
ViSER	15.7	52.2	23.0	20.6	16.8	21.3
Ours ^S	9.4	56.8	10.8	48.6	10.5	35.2
Nerfies ^S	22.6	13.2	18.4	18.0	24.4	14.9

tances and F-scores. Chamfer distance computes the average distance between the ground-truth and the estimated surface points by finding the nearest neighbour matches, but it is sensitive to outliers. Therefore, we further report the F-score at distance thresholds $d = 2\%$ of the longest edge of the axis-aligned object bounding box [51]. To account for the unknown scale and global rigid motion, we pre-align the estimated shape to the ground-truth via Iterative Closest Point (ICP) up to a 3D similarity transformation.

4.2. Reconstruction Results

We show qualitative comparison in Fig. 4 and quantitative comparison in Tab. 1.

Baseline setup. Nerfies [33] is designed for a single continuously captured video, assuming object root body pose can be compensated by background-SfM. In our setup, object moves and background SfM does not provide root poses for the object. When focused on the deformable object, SfM (such as COLMAP) failed to converge due to violation of rigidity, leading to very few successful registrations (18 over 900 images registered on *casual-cat*). To make a fair comparison, we provide Nerfies with rough initial root poses (obtained from our PoseNet, Sec. 3.4). After optimization, meshes are extracted by running marching cubes on a 256^3 grid. Another baseline, ViSER [65], directly optimizes object shape and poses using optical flow, silhouette, and color reconstruction losses. It does not assume category-level priors such as CSE features, and therefore applicable to generic object categories. However, ViSER’s root pose estimation is sensitive to large deformation and a large number of input frames (more than 20). Since it produces worse results than our PoseNet, we provide ViSER the same root poses from our initialization pipeline.

Comparison with Nerfies. Nerfies optimizes SE(3) fields with photometric error, which fails at large motion and fails to register pixels across videos. In contrast, BANMo optimizes an articulated bones model using *featuremetric* consistency w.r.t. a pre-trained CSE feature embedding. As

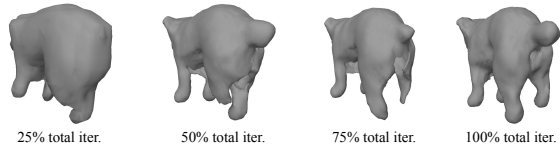


Figure 5. **Compliance to topology changes in optimization.** BANMo incorrectly reconstructs a single rear leg of the dog, but automatically corrects the topology with gradient updates.

shown in Fig. 4, although single-video Nerfies reconstructs reasonable 3D shapes of moving objects given rough initial root pose, it fails to reconstruct large articulations, such as the fast motion of the cat’s head (2nd row). Furthermore, as shown in Fig. 9, Nerfies is not able to leverage more videos to improve the reconstruction quality, while the reconstruction of BANMo improves given more videos. The results in Tab. 1 suggests BANMo produces more accurate geometry than Nerfies for all sequences.

Comparison with ViSER. As shown in Fig. 4, ViSER produces reasonable articulated shapes. However, detailed geometry, such as ears, eyes, nose and rear limbs of the cat are blurred out. Furthermore, detailed articulation, such as head rotation and leg switching are not recovered. In contrast, BANMo faithfully recovers these high-fidelity geometry and motion. We observed that the neural implicit volume representation is compliant to topology changes during gradient updates (see Fig. 5), and is therefore able to recover from bad local optima. In contrast, sub-optimal topology that happens during optimization, such as inverted faces, prevents ViSER to improve given more iterations. Compared to meshes with finite number of vertices, implicit shape representation maintains a continuous geometry, enabling us to recover detailed shape without additional cost in rendering high-res meshes.

4.3. Diagnostics

We ablate the importance of each component, by using a subset of videos. To also ablate root pose initialization and registration, we test on AMA’s *samba* and *swing* (325 frames in total). We include exhaustive ablations in supplement, and only highlight crucial aspects of BANMo below.

Root pose initialization. We show the effect of PoseNet for root pose initialization (Sec 3.4) in Fig. 6: without it, the root poses (or equivalently camera poses) collapsed to a degenerate solution after optimization.

Registration. In Fig. 7, we show the benefit of using canonical embeddings (Sec 3.3), and measured 2D flow (Eq. 16) to register observations across videos and within a video. Without the canonical embeddings and corresponding losses (Eq. 17-18), each video will be reconstructed separately. With no flow reconstruction loss, multiple ghosting structures are reconstructed due to failed registration.

Deformation modeling. We demonstrate the benefit of us-

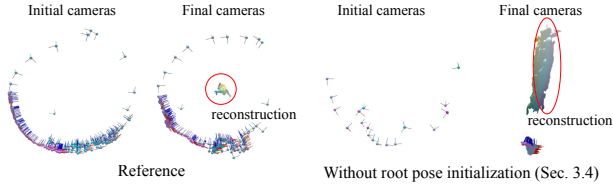


Figure 6. **Diagnostics of root pose initialization (Sec.3.4)**. With randomly initialized root poses, the estimated poses (on the right) collapsed to a degenerate solution, causing reconstruction to fail.

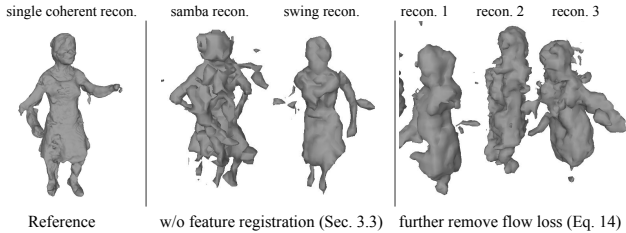


Figure 7. **Diagnostics of registration (Sec. 3.3)**. Without canonical embeddings (middle) or flow loss (right), our method fails to register frames to a canonical model, creating ghosting effects.



Figure 8. **Diagnostics of deformation modeling (Sec.3.2)**. Replacing our neural blend skinning with MLP-SE(3) results in less regular deformation in the non-visible region. Replacing our neural blend skinning with MLP-translation as in NSFF and D-NeRF results in reconstructing ghosting wings due to significant motion.

ing our neural blend skinning model (Sec 3.2) on an eagle sequence, which is challenging due to its large wing articulations. If we swap neural blend skinning for MLP-SE(3) [33], the reconstruction is less regular. If we swap for MLP-translation [22, 38], we observe ghosting wings due to wrong geometric registration (caused by large motion). Our method can model large articulations thanks to the regularization from the Gaussian component, and also handle complex deformation such as close contact of hands.

Ability to leverage more videos. We compare BANMo to Nerfies in its ability to leverage more available video observations. To demonstrate this, we compare the reconstruction quality of optimizing 1 video vs. 8 videos from the AMA samba sequences. As shown in Fig. 9, given more videos, our method can register them to the same canonical space, improving the reconstruction completeness and reducing shape ambiguities. In contrast, Nerfies does not produce better results given more video observations.

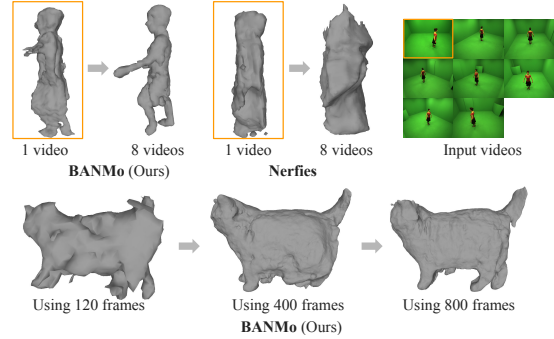


Figure 9. **Reconstruction completeness vs number of input videos and video frames.** BANMo is capable of registering more input videos if they are available, improving the reconstruction.

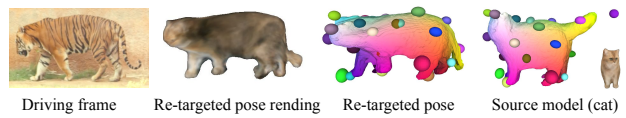


Figure 10. **Motion re-targeting from a pre-optimized cat model to a tiger.** Color coded by point locations in the canonical space.

4.4. Application: Motion retargeting

As a distinctive application, we demonstrate BANMo’s ability of to re-target the articulations of a driving video to our 3D model by optimizing the frame-specific root and body pose codes ω_r^t , ω_b^t , as shown in Fig. 10. To do so, we first optimize all parameters over a set of *training* videos from our *casual-cat* dataset. Given a driving video of a tiger, we freeze the shared model parameters (including shape, skinning, and canonical features) of the cat model, and only optimize the video-specific and frame-specific codes, i.e. root and body pose codes ω_r^t , ω_b^t , as well as the environment lighting code ω_e^t .

5. Discussion

We have presented BANMo, a method to reconstruct high-fidelity animatable 3D models from a collection of casual videos, without requiring a pre-defined shape template or pre-registered cameras. BANMo registers thousands of *unsynchronized* video frames to the same canonical space by enforcing feature-metric consistencies via 2D-3D correspondence matching. We have also shown benefits of using a hybrid neural blend-skinning model for reconstructing large deformations and fine geometry.

Limitations. BANMo uses a pre-trained DensePose-CSE (with 2D keypoint annotations [31]) to provide rough root body pose registration. To build generic pipelines of deformable 3D model reconstruction, a generic relative root pose estimator is needed. Similar to other works in differentiable rendering, BANMo requires a lot of compute, which increases linearly with the number of input images. We leave speeding up the optimization as future work.

A. Notations

We refer readers to a list of notations in Tab. 6 and a list of learnable parameters in Tab. 7. We compare with Nerfies and ViSER and summarize the differences in Tab. 2.

Table 2. **Difference between Nerfies, ViSER, and BANMo.**

Method	shape	deformation	registration
Nerfies	implicit	dense SE(3)	photometric
ViSER	mesh	control points	self-supervised feature
BANMo	implicit	control points	pre-trained feature

B. Method details

B.1. Root Pose Initialization

As discussed in Sec. 3.4, to make optimization robust, we train a image CNN (denoted as PoseNet) to initialize root body transforms \mathbf{G}^t that aligns the camera space of time t to the canonical space of CSE, as shown in Fig. 11.

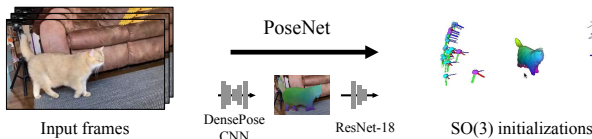


Figure 11. **Inference pipeline of PoseNet.** To initialize the optimization, we train a CNN PoseNet to predict root poses given a single image. PoseNet uses a DensePose-CNN to extract pixel features and decodes the pixel features into root pose predictions with a ResNet-18. We visualize the initial root poses on the right. Cyan color represents earlier time stamps and magenta color represent later timestamps.

Preliminary DensePose CSE [30, 31] trains pixel embeddings ψ_I and surface feature embeddings ψ for humans and quadruped animals using 2D keypoint annotations. It represents surface embeddings by a canonical surface with N vertices and vertex features $\psi \in \mathbb{R}^{N \times 16}$. A SMPL mesh is used for humans, and a sheep mesh is used for quadruped animals. The embeddings are trained such that given a pixel feature, a 3D point on the canonical surface can be uniquely located via feature matching.

Naive PnP solution Given 2D-3D correspondences provided by CSE, one way to solve for \mathbf{G}^t is to use perspective-n-points (PnP) algorithm assuming objects are rigid. However, the PnP solution suffers from catastrophic failures due to the non-rigidity of the object, which motivates our PoseNet solution. By training a feed-forward network with data augmentations, our PoseNet solution produces fewer gross errors than the naive PnP solution.

Synthetic dataset genearion. We train separate PoseNet, one for human, and one for quadruped animals. The training pipeline is shown in Fig. 12. Specifically, we render sur-

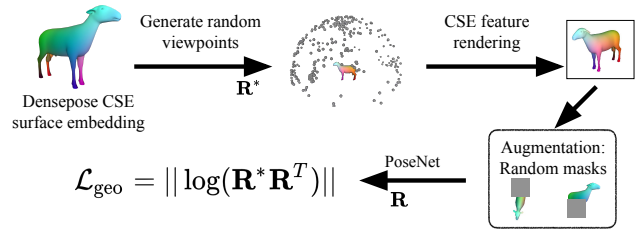


Figure 12. **Training pipeline of PoseNet.** To train PoseNet, we use DesePose CSE surface embeddings, which is pertained on 2D annotations of human and quadruped animals. We first generate random viewpoints on a sphere that faces the origin. Then we render surface embeddings as 16-channel images. We further augment the feature images with random adversarial masks to improve the robustness to occlusions. Finally, the rotations predicted by PoseNet are compared against the ground-truth rotations with geodesic distance.

face features as feature images $\psi_{\text{rnd}} \in \mathbb{R}^{112 \times 112 \times 16}$ given viewpoints $\mathbf{G}^* = (\mathbf{R}^*, \mathbf{T}^*)$ randomly generated on a unit sphere facing the origin. We apply occlusion augmentations [44] that randomly mask out a rectangular region in the rendered feature image and replace with mean values of the corresponding feature channels. The random occlusion augmentation forces the network to be robust to outlier inputs, and empirically helps network to make robust predictions in presence of occlusions and in case of out-of-distribution appearance.

Loss and inference. We use the geodesic distance between the ground-truth and predicted rotations as a loss to update PoseNet,

$$\mathcal{L}_{\text{geo}} = \|\log(\mathbf{R}^* \mathbf{R}^T)\|, \quad \mathbf{R} = \text{PoseNet}(\psi_{\text{rnd}}), \quad (21)$$

where we find learning to predict rotation is sufficient for initializing the root body pose. In practice, we set the initial object-to-camera translation to be a constant $\mathbf{T} = (0, 0, 3)^T$. We run pose CNN on each test video frame to obtain the initial root poses $\mathbf{G}_0^t = (\mathbf{R}, \mathbf{T})$, and compute a delta root pose with the root pose MLP:

$$\mathbf{G}^t = \text{MLP}_{\mathbf{G}}(\omega_r^t) \mathbf{G}_0^t. \quad (22)$$

B.2. Active sampling over (x, y, t)

Inspired by iMAP [48], our ray sampling strategy follows an easy-to-hard curriculum. At the early iterations, we randomly sample a batch of N^p pixels for volume rendering and compute reconstruction losses. At the same time, we optimize a 8-layer MLP function to represent the uncertainty over the image coordinate and frame index: $\hat{\mathbf{U}}(x, y, t) = \text{MLP}_{\mathbf{U}}(x, y, t)$. The uncertainty MLP is optimized by comparing against the color reconstruction er-

Table 3. Table of hyper-parameters.

Name	Value	Description
B	25	Number of bones
N	128	Sampled points per ray
N^p	6144	Sampled rays per batch
(H, W)	(512,512)	Resolution of observed images

rors in the current forward step:

$$\mathcal{L}_U = \sum_{\mathbf{x}, t} \left\| \mathcal{L}_{\text{rgb}}(\mathbf{x}^t) - \hat{U}(\mathbf{x}^t) \right\|. \quad (23)$$

Note that the gradient from \mathcal{L}_U to $\mathcal{L}_{\text{rgb}}(\mathbf{x}^t)$ is stopped such that \mathcal{L}_U does not generate gradients to parameters besides MLP_U . After some optimization steps, we replace half of the samples with *active* samples from pixels with high uncertainties. To do so, we randomly sample $N^{a'} = 24576$ pixels, and evaluate their uncertainties by passing their coordinates and frame indices to MLP_U . Active samples dramatically improves reconstruction fidelity, as shown in Fig. 16.

B.3. Optimization details

Canonical 3D grid. As mentioned in Sec 3.3, we define a canonical 3D grid $\mathbf{V}^* \in \mathbb{R}^{20 \times 20 \times 20}$ to compute the matching costs between pixels and canonical space locations. The canonical grid is centered at the origin and axis-aligned with bounds $[x_{\min}, x_{\max}]$, $[y_{\min}, y_{\max}]$, and $[z_{\min}, z_{\max}]$. The bounds are initialized as loose bounds and are refined during optimization. For every 200 iterations, we update the bounds of the canonical volume as an approximate bound of the object surface. To do so, we run marching cubes on a 64^3 grid to extract a surface mesh and then set L as the axis-aligned (x, y, z) bounds of the extracted surface.

Near-far planes. To generate samples for volume rendering, we dynamically compute the depth of near-far planes (d_n^t, d_f^t) of frame t at each iterations of the optimization. To do so, we compute the projected depth of the canonical surface points $d_i^t = (\Pi^t \mathbf{G}^t \mathbf{X}_i^*)_2$. The near plane is set as $d_n^t = \min(d_i) - \epsilon_L$ and the far plane is set as $d_f^t = \max(d_i) + \epsilon_L$, where $\epsilon_L = 0.2(\max(d_i) - \min(d_i))$. To avoid the compute overhead, we approximate the surface with an axis-aligned bounding box with 8 points.

Hyper-parameters. We use **1cycle** learning rate scheduler, which warms-up with a low learning rate to the maximum, and anneals the learning rate to a final learning rate. We apply $lr_{\text{init}} = 2e - 5$, $lr_{\text{max}} = 5e - 4$, $lr_{\text{final}} = 1e - 4$. We refer readers to a complete list of hyper-parameters in Tab. 3.

Multi-stage optimization The final optimization takes three stages, where the optimizable parameters and the loss

functions used are different. The first stage uses all the losses and updates all the parameters described in the paper. Typically, the first stage already produces 3D reconstructions with good shape and deformation. The goal of the stage 2 is to improve the articulations (e.g., to correctly articulate the crossing legs for `cat-pikachu`) with coordinate gradient descent, where we turn off the reconstruction losses and only use the 2D cycle consistency loss to update the articulation parameters while keeping shape parameters fixed. Finally, stage 3 improves the details of the geometry by active sampling and importance depth sampling while keeping the root body poses fixed.

Experiment details When running Nerfies on AMA and animated objects, we found using RGB reconstruction loss does not produce meaningful results possibly due to the homogeneous background color. To improve Nerfies results, we provide it with ground-truth object silhouettes, and optimize a carefully balanced RGB+silhouette loss [67].

C. Additional results

C.1. SFM root pose initialization

COLMAP [41, 42] failed to converge when focused on the deformable object due to violation of rigidity, leading to very few successful registrations (18 over 811 images registered on `casual-cat`). A recent end-to-end method, DROID-SLAM [52], registered all the images but the accuracy is low compared to PoseNet, as shown in Tab. 4. We also tried SFM to estimate and compensate for the camera motion (using background as rigid anchor), but this did not help to recover the pose of the object due to its global movement w.r.t. to the background.

Table 4. **Evaluation on root pose prediction.** Mean and standard deviation of the rotation error ($^\circ$) over all frames (\downarrow). We use BANMo-optimized poses as ground-truth. Rotations are aligned to the ground-truth by a global rotation under **chordal L2 distance**.

Method	c-cat	c-human	ama-human
CSE-PoseNet	18.6 \pm 16.2	12.8 \pm 8.9	11.8 \pm 17.4
DROID-SLAM	65.5 \pm 44.5	55.8 \pm 39.2	83.6 \pm 50.5

C.2. More ablation study

In Sec. 4.3, we presented qualitative results of diagnostics experiments. In Tab. 5, we report the results of other ablations followed by analysis.

Number and location of bones As shown in the first group of Tab. 5 and Fig. 13, using too few bones fails to recover all body parts due to over-regularization. Using more than 16 bones produces good reconstructions, but consumes more memory when computing skinning weights. Enforcing them to stay close to the surface with a **sinkhorn divergence loss** improves the results (Tab. 5, L16-17).

Table 5. **Results on AMA swing and samba.** 3D Chamfer distance (cm, ↓) and F-score (% , ↑) averaged over all frames.

Method	CD	F@1%	F@2%	F@5%
number-bone=4	9.88	28.1	52.4	84.1
number-bone=9	9.08	31.2	56.4	86.8
number-bone=16	9.02	31.8	57.2	87.2
number-bone=25	9.08	31.8	57.0	87.1
-w/o in-surface loss	9.14	29.9	54.8	86.7
-quad. embedding	9.70	29.8	54.2	85.4
number-bone=64	9.18	31.1	56.6	87.5
number-bone=100	9.11	31.4	56.7	87.3
pose error $\epsilon=20^\circ$	8.75	30.9	57.0	88.1
pose error $\epsilon=50^\circ$	8.91	29.8	56.1	88.1
pose error $\epsilon=90^\circ$	9.91	28.4	54.8	85.7
coverage=90° (2 vids)	10.61	29.3	54.3	84.1
coverage=180° (4 vids)	8.94	33.0	59.8	87.9
coverage=270° (6 vids)	9.09	29.8	56.1	87.6
active-sample=0%	9.63	29.1	53.7	85.8
active-sample=25%	8.60	32.3	57.9	88.0
active-sample=50%	9.14	29.9	54.8	86.7

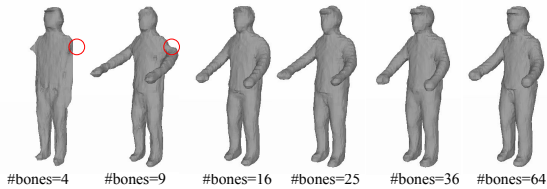


Figure 13. **Sensitivity to number of bones.**

Sensitivity to incorrect initial pose We inject different levels of Gaussian noise into the initial poses, leading to average rotation errors $\epsilon \in \{20, 50, 90\}^\circ$. As shown in the second group of Tab. 5, BANMo is stable up to 50° rotation error.

Pre-trained embeddings Pre-trained embeddings help BANMo outperform Nerfies, but it is not crucial given good initial root poses ($\epsilon = 12.8 \pm 8.9^\circ$). As shown in Tab. 5, using embeddings pre-trained for quadruped animals for human optimization produces slightly worse results.

How much data are needed? To reconstruct a complete shape, BANMo requires all object surface to be visible from at least one frame. Beside completeness, more videos allows to estimate better skinning weights and a more regular motion. We evaluate view coverage in the third group of Tab. 5.

Importance sampling We use active sampling to avoid sampling from uninformative frames and pixels. It consistently improves reconstruction results as shown in the last group of Tab. 5.

Bone re-initialization We qualitatively evaluate the effect of rest bone re-initialization, which re-initializes bone pa-

rameters according to the current estimation of shape. As shown in Fig. 14, without re-initializing the bones, the optimization may stuck at bad local optima and the final reconstruction may become less accurate.

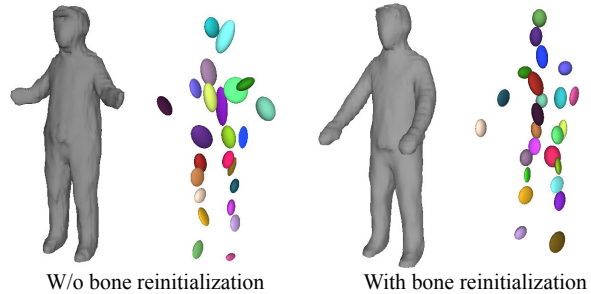


Figure 14. **Effect of bone re-initialization.** We find it important to re-initialize rest bone parameters after finding a better approximation of object geometry.

Delta skinning weights We qualitatively evaluate the effect of delta skinning weights. As shown in Fig. 15, without learning a delta skinning weights specific to each 3D point, the reconstructed shape and motion may be over-regularized by the 3D Gaussians.

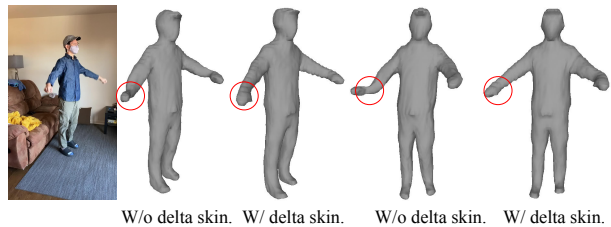


Figure 15. **Effect of delta skinning weights.** We find it important to learn a point-specific delta skinning weight function to reconstruction motions in high-quality.

Active sampling. We show the effect of active sampling on a casual-cat video (Fig. 16): removing it results in slower convergence and inaccurate geometry.

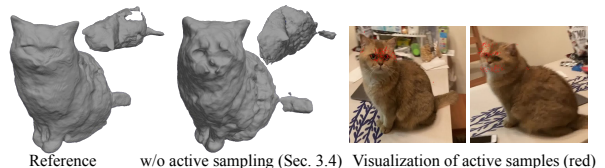


Figure 16. **Diagnostics of active sampling over (x, y) .** With no active sampling, our method converges slower and misses details (such as ears and eyes). Active samples focus on face and boundaries pixels where the color reconstruction errors are higher.

C.3. Qualitative results

We refer readers to our supplementary webpage for complete qualitative results.

Table 6. Table of notations.

Symbol	Description
Index	
t	Frame index, $t \in \{1, \dots, T\}$
b	Bone index $b \in \{1, \dots, B\}$ in neural blend skinning
i	Point index $b \in \{1, \dots, N\}$ in volume rendering
Points	
\mathbf{x}	Pixel coordinate $\mathbf{x} = (x, y)$
\mathbf{X}^t	3D point locations in the frame t camera coordinate
\mathbf{X}^*	3D point locations in the canonical coordinate
$\hat{\mathbf{X}}^*$	Matched canonical 3D point locations via canonical embedding
Property of 3D points	
$\mathbf{c} \in \mathbb{R}^3$	Color of a 3D point
$\sigma \in \mathbb{R}$	Density of a 3D point
$\psi \in \mathbb{R}^{16}$	Canonical embedding of a 3D point
$\mathbf{W} \in \mathbb{R}^B$	Skinning weights of assigning a 3D point to B bones
Functions on 3D points	
$\mathcal{W}^{t, \leftarrow}(\mathbf{X}^t)$	Backward warping function from \mathbf{X}^t to \mathbf{X}^*
$\mathcal{W}^{t, \rightarrow}(\mathbf{X}^*)$	Forward warping function from \mathbf{X}^* to \mathbf{X}^t
$\mathcal{S}(\mathbf{X}, \omega_b)$	Skinning function that computes skinning weights of \mathbf{X} under body pose ω_b
Rendered and Observed Images	
$\mathbf{c}/\hat{\mathbf{c}}$	Rendered/observed RGB image
$\mathbf{o}/\hat{\mathbf{s}}$	Rendered/observed object silhouette image
$\mathcal{F}/\hat{\mathcal{F}}$	Rendered/observed optical flow image

Table 7. Table of learnable parameters.

Symbol	Description
Canonical Model Parameters	
MLP_c	Color MLP
MLP_{SDF}	Shape MLP
MLP_ψ	Canonical embedding MLP
Deformation Model Parameters	
$\Lambda^0 \in \mathbb{R}^{3 \times 3}$	Scale of the bones in the zero-configuration (diagonal matrix).
$\mathbf{V}^0 \in \mathbb{R}^{3 \times 3}$	Orientation of the bones in the zero-configuration.
$\mathbf{C}^0 \in \mathbb{R}^3$	Center of the bones in the zero-configuration.
MLP_Δ	Delta skinning weight MLP
MLP_G	Root pose MLP
MLP_J	Body pose MLP
Learnable Codes	
$\omega_b^* \in \mathbb{R}^{128}$	Body pose code for the rest pose
$\omega_b^t \in \mathbb{R}^{128}$	Body pose code for frame t
$\omega_r^t \in \mathbb{R}^{128}$	Root pose code for frame t
$\omega_e^t \in \mathbb{R}^{64}$	Environment lighting code for frame t , shared across frames of the same video
Other Learnable Parameters	
ψ_I	CNN pixel embedding initialized from DensePose CSE
α_s	Temperature scalar for canonical feature matching
β	Scale parameter that controls the solidness of the object surface
$\Pi \in \mathbb{R}^{3 \times 3}$	Intrinsic matrix of the pinhole camera model

References

- [1] Sameer Agarwal, Yasutaka Furukawa, Noah Snavely, Ian Simon, Brian Curless, Steven M Seitz, and Richard Szeliski. Building rome in a day. *Communications of the ACM*, 2011. 1
- [2] Marc Badger, Yufu Wang, Adarsh Modh, Ammon Perkes, Nikos Kolotouros, Bernd Pfrommer, Marc Schmidt, and Kostas Daniilidis. 3D bird reconstruction: a dataset, model, and shape recovery from a single view. In *ECCV*, 2020. 2
- [3] Benjamin Biggs, Ollie Boyne, James Charles, Andrew Fitzgibbon, and Roberto Cipolla. Who left the dogs out: 3D animal reconstruction with expectation maximization in the loop. In *ECCV*, 2020. 2
- [4] Christoph Breger, Aaron Hertzmann, and Henning Biermann. Recovering non-rigid 3d shape from image streams. In *CVPR*, 2000. 2
- [5] Xu Chen, Yufeng Zheng, Michael J Black, Otmar Hilliges, and Andreas Geiger. Snarf: Differentiable forward skinning for animating non-rigid neural implicit shapes. 2021. 2, 4
- [6] Jean Feydy, Thibault Séjourné, François-Xavier Vialard, Shun-ichi Amari, Alain Trounev, and Gabriel Peyré. Interpolating between optimal transport and mmd using sinkhorn divergences. In *The 22nd International Conference on Artificial Intelligence and Statistics*, pages 2681–2690, 2019. 6
- [7] Shubham Goel, Angjoo Kanazawa, and Jitendra Malik. Shape and viewpoints without keypoints. In *ECCV*, 2020. 2
- [8] Paulo FU Gotardo and Aleix M Martinez. Non-rigid structure from motion with complementary rank-3 spaces. In *CVPR*, 2011. 2
- [9] Alec Jacobson, Zhigang Deng, Ladislav Kavan, and JP Lewis. Skinning: Real-time shape deformation. In *ACM SIGGRAPH 2014 Courses*, 2014. 4
- [10] Yasamin Jafarian and Hyun Soo Park. Learning high fidelity depths of dressed humans by watching social media dance videos. In *CVPR*, pages 12753–12762, June 2021. 2
- [11] Yoonwoo Jeong, Seokjun Ahn, Christopher Choy, Anima Anandkumar, Minsu Cho, and Jaesik Park. Self-calibrating neural radiance fields. In *ICCV*, 2021. 2
- [12] Angjoo Kanazawa, Shubham Tulsiani, Alexei A. Efros, and Jitendra Malik. Learning category-specific mesh reconstruction from image collections. In *ECCV*, 2018. 2
- [13] Alex Kendall, Hayk Martirosyan, Saumitro Dasgupta, Peter Henry, Ryan Kennedy, Abraham Bachrach, and Adam Bry. End-to-end learning of geometry and context for deep stereo regression. In *ICCV*, 2017. 5
- [14] Alexander Kirillov, Yuxin Wu, Kaiming He, and Ross Girshick. Pointrend: Image segmentation as rendering. In *CVPR*, 2020. 6
- [15] Muhammed Kocabas, Nikos Athanasiou, and Michael J. Black. Vibe: Video inference for human body pose and shape estimation. In *CVPR*, June 2020. 2
- [16] Filippos Kokkinos and Iasonas Kokkinos. To the point: Correspondence-driven monocular 3d category reconstruction. In *NeurIPS*, 2021. 2
- [17] Chen Kong and Simon Lucey. Deep non-rigid structure from motion. In *ICCV*, 2019. 2
- [18] Nilesh Kulkarni, Abhinav Gupta, David F Fouhey, and Shubham Tulsiani. Articulation-aware canonical surface mapping. In *CVPR*, pages 452–461, 2020. 2, 5
- [19] Suryansh Kumar. Non-rigid structure from motion: Prior-free factorization method revisited. In *WACV*, 2020. 2
- [20] Xueting Li, Sifei Liu, Shalini De Mello, Kihwan Kim, Xiaolong Wang, Ming-Hsuan Yang, and Jan Kautz. Online adaptation for consistent mesh reconstruction in the wild. In *NeurIPS*, 2020. 2
- [21] Xueting Li, Sifei Liu, Kihwan Kim, Shalini De Mello, Varun Jampani, Ming-Hsuan Yang, and Jan Kautz. Self-supervised single-view 3d reconstruction via semantic consistency. *ECCV*, 2020. 2
- [22] Zhengqi Li, Simon Niklaus, Noah Snavely, and Oliver Wang. Neural scene flow fields for space-time view synthesis of dynamic scenes. In *CVPR*, 2021. 2, 3, 5, 6, 8
- [23] Chen-Hsuan Lin, Wei-Chiu Ma, Antonio Torralba, and Simon Lucey. Barf: Bundle-adjusting neural radiance fields. In *ICCV*, 2021. 2
- [24] Lingjie Liu, Marc Habermann, Viktor Rudnev, Kripasindhu Sarkar, Jiatao Gu, and Christian Theobalt. Neural actor: Neural free-view synthesis of human actors with pose control. *SIGGRAPH Asia*, 2021. 2
- [25] Matthew Loper, Naureen Mahmood, Javier Romero, Gerard Pons-Moll, and Michael J. Black. SMPL: A skinned multi-person linear model. *SIGGRAPH Asia*, 2015. 2
- [26] Diogo C Luvizon, Hedi Tabia, and David Picard. Human pose regression by combining indirect part detection and contextual information. *Computers & Graphics*, 2019. 5
- [27] Ricardo Martin-Brualla, Noha Radwan, Mehdi S. M. Sajjadi, Jonathan T. Barron, Alexey Dosovitskiy, and Daniel Duckworth. NeRF in the Wild: Neural Radiance Fields for Unconstrained Photo Collections. In *CVPR*, 2021. 2, 3
- [28] Quan Meng, Anpei Chen, Haimin Luo, Minye Wu, Hao Su, Lan Xu, Xuming He, and Jingyi Yu. Gnerf: Gan-based neural radiance field without posed camera. In *ICCV*, 2021. 2
- [29] Ben Mildenhall, Pratul P Srinivasan, Matthew Tancik, Jonathan T Barron, Ravi Ramamoorthi, and Ren Ng. Nerf: Representing scenes as neural radiance fields for view synthesis. In *ECCV*, 2020. 2, 3, 5, 6
- [30] Natalia Neverova, David Novotny, Vasil Khalidov, Marc Szafraniec, Patrick Labatut, and Andrea Vedaldi. Continuous surface embeddings. In *NeurIPS*, 2020. 3, 4, 5, 6, 9
- [31] Natalia Neverova, Arsiom Sanakoyeu, Patrick Labatut, David Novotny, and Andrea Vedaldi. Discovering relationships between object categories via universal canonical maps. In *CVPR*, 2021. 4, 8, 9
- [32] Atsuhiko Noguchi, Xiao Sun, Stephen Lin, and Tatsuya Harada. Neural articulated radiance field. In *ICCV*, 2021. 2
- [33] Keunhong Park, Utkarsh Sinha, Jonathan T. Barron, Sofien Bouaziz, Dan B Goldman, Steven M. Seitz, and Ricardo Martin-Brualla. Nerfies: Deformable neural radiance fields. In *ICCV*, 2021. 2, 3, 6, 7, 8

- [34] Keunhong Park, Utkarsh Sinha, Peter Hedman, Jonathan T. Barron, Sofien Bouaziz, Dan B Goldman, Ricardo Martin-Brualla, and Steven M. Seitz. Hypernerf: A higher-dimensional representation for topologically varying neural radiance fields. *arXiv*, 2021. 2
- [35] Georgios Pavlakos, Vasileios Choutas, Nima Ghorbani, Timo Bolkart, Ahmed A. A. Osman, Dimitrios Tzionas, and Michael J. Black. Expressive body capture: 3d hands, face, and body from a single image. In *CVPR*, 2019. 2
- [36] Sida Peng, Junting Dong, Qianqian Wang, Shangzhan Zhang, Qing Shuai, Xiaowei Zhou, and Hujun Bao. Animatable neural radiance fields for modeling dynamic human bodies. In *ICCV*, 2021. 2
- [37] Sida Peng, Yuanqing Zhang, Yinghao Xu, Qianqian Wang, Qing Shuai, Hujun Bao, and Xiaowei Zhou. Neural body: Implicit neural representations with structured latent codes for novel view synthesis of dynamic humans. In *CVPR*, 2021. 2
- [38] Albert Pumarola, Enric Corona, Gerard Pons-Moll, and Francesc Moreno-Noguer. D-NeRF: Neural Radiance Fields for Dynamic Scenes. In *CVPR*, 2020. 2, 8
- [39] Shunsuke Saito, Jinlong Yang, Qianli Ma, and Michael J. Black. SCANimate: Weakly supervised learning of skinned clothed avatar networks. In *CVPR*, 2021. 2, 4
- [40] Peter Sand and Seth Teller. Particle video: Long-range motion estimation using point trajectories. In *IJCV*, 2008. 2
- [41] Johannes Lutz Schönberger and Jan-Michael Frahm. Structure-from-motion revisited. In *CVPR*, 2016. 10
- [42] Johannes Lutz Schönberger, Enliang Zheng, Marc Pollefeys, and Jan-Michael Frahm. Pixelwise view selection for unstructured multi-view stereo. In *European Conference on Computer Vision (ECCV)*, 2016. 10
- [43] Vikramjit Sidhu, Edgar Tretschk, Vladislav Golyanik, Antonio Agudo, and Christian Theobalt. Neural dense non-rigid structure from motion with latent space constraints. In *ECCV*, 2020. 2
- [44] Krishna Kumar Singh and Yong Jae Lee. Hide-and-seek: Forcing a network to be meticulous for weakly-supervised object and action localization. In *ICCV*, 2017. 9
- [45] Noah Snavely, Steven M Seitz, and Richard Szeliski. Photo tourism: exploring photo collections in 3d. In *SIGGRAPH*. 2006. 1
- [46] Noah Snavely, Steven M Seitz, and Richard Szeliski. Modeling the world from internet photo collections. *IJCV*, 2008. 1
- [47] Shih-Yang Su, Frank Yu, Michael Zollhöfer, and Helge Rhodin. A-nerf: Articulated neural radiance fields for learning human shape, appearance, and pose. In *NeurIPS*, 2021. 2
- [48] Edgar Sucar, Shikun Liu, Joseph Ortiz, and Andrew Davison. iMAP: Implicit mapping and positioning in real-time. In *ICCV*, 2021. 9
- [49] Narayanan Sundaram, Thomas Brox, and Kurt Keutzer. Dense point trajectories by gpu-accelerated large displacement optical flow. In *ECCV*, 2010. 2
- [50] Matthew Tancik, Pratul P. Srinivasan, Ben Mildenhall, Sara Fridovich-Keil, Nithin Raghavan, Utkarsh Singhal, Ravi Ramamoorthi, Jonathan T. Barron, and Ren Ng. Fourier features let networks learn high frequency functions in low dimensional domains. *NeurIPS*, 2020. 4
- [51] Maxim Tatarchenko, Stephan R Richter, René Ranftl, Zhuwen Li, Vladlen Koltun, and Thomas Brox. What do single-view 3d reconstruction networks learn? In *CVPR*, pages 3405–3414, 2019. 7
- [52] Zachary Teed and Jia Deng. Droid-slam: Deep visual slam for monocular, stereo, and rgb-d cameras. *Advances in Neural Information Processing Systems*, 34, 2021. 10
- [53] Edgar Tretschk, Ayush Tewari, Vladislav Golyanik, Michael Zollhöfer, Christoph Lassner, and Christian Theobalt. Non-rigid neural radiance fields: Reconstruction and novel view synthesis of a dynamic scene from monocular video. In *ICCV*, 2021. 2
- [54] Shubham Tulsiani, Nilesh Kulkarni, and Abhinav Gupta. Implicit mesh reconstruction from unannotated image collections. In *arXiv*, 2020. 2
- [55] Daniel Vlasic, Ilya Baran, Wojciech Matusik, and Jovan Popović. Articulated mesh animation from multi-view silhouettes. *TOG*, 2008. 6
- [56] Minh Vo, Yaser Sheikh, and Srinivasa G Narasimhan. Spatiotemporal bundle adjustment for dynamic 3d human reconstruction in the wild. *IEEE TPAMI*, 2020. 2
- [57] Chaoyang Wang, Ben Eckart, Simon Lucey, and Orazio Gallo. Neural trajectory fields for dynamic novel view synthesis. *arXiv preprint arXiv:2105.05994*, 2021. 2
- [58] Peng Wang, Lingjie Liu, Yuan Liu, Christian Theobalt, Taku Komura, and Wenping Wang. Neus: Learning neural implicit surfaces by volume rendering for multi-view reconstruction. *NeurIPS*, 2021. 3
- [59] Zirui Wang, Shangzhe Wu, Weidi Xie, Min Chen, and Victor Adrian Prisacariu. Nerf-: Neural radiance fields without known camera parameters. In *arXiv preprint arXiv:2102.07064*, 2021. 2
- [60] Shangzhe Wu, Tomas Jakab, Christian Rupprecht, and Andrea Vedaldi. Dove: Learning deformable 3d objects by watching videos. *arXiv preprint arXiv:2107.10844*, 2021. 2
- [61] Donglai Xiang, Hanbyul Joo, and Yaser Sheikh. Monocular total capture: Posing face, body, and hands in the wild. In *CVPR*, 2019. 2
- [62] Yuanlu Xu, Song-Chun Zhu, and Tony Tung. Denserac: Joint 3d pose and shape estimation by dense render-and-compare. In *ICCV*, 2019. 5
- [63] Gengshan Yang and Deva Ramanan. Volumetric correspondence networks for optical flow. In *NeurIPS*, 2019. 6
- [64] Gengshan Yang, Deqing Sun, Varun Jampani, Daniel Vlasic, Forrester Cole, Huiwen Chang, Deva Ramanan, William T Freeman, and Ce Liu. LASR: Learning articulated shape reconstruction from a monocular video. In *CVPR*, 2021. 2, 4
- [65] Gengshan Yang, Deqing Sun, Varun Jampani, Daniel Vlasic, Forrester Cole, Ce Liu, and Deva Ramanan. Viser: Video-specific surface embeddings for articulated 3d shape reconstruction. In *NeurIPS*, 2021. 2, 4, 5, 6, 7

- [66] Lior Yariv, Jiatao Gu, Yoni Kasten, and Yaron Lipman. Volume rendering of neural implicit surfaces. *arXiv preprint arXiv:2106.12052*, 2021. 3
- [67] Lior Yariv, Yoni Kasten, Dror Moran, Meirav Galun, Matan Atzmon, Basri Ronen, and Yaron Lipman. Multiview neural surface reconstruction by disentangling geometry and appearance. In *NeurIPS*, 2020. 5, 6, 10
- [68] Yufei Ye, Shubham Tulsiani, and Abhinav Gupta. Shelf-supervised mesh prediction in the wild. In *CVPR*, 2021. 2
- [69] Jason Y. Zhang, Gengshan Yang, Shubham Tulsiani, and Deva Ramanan. NeRS: Neural reflectance surfaces for sparse-view 3d reconstruction in the wild. In *NeurIPS*, 2021. 5
- [70] Tiancheng Zhi, Christoph Lassner, Tony Tung, Carsten Stoll, Srinivasa G Narasimhan, and Minh Vo. Texmesh: Reconstructing detailed human texture and geometry from rgb-d video. In *ECCV*, 2020. 2
- [71] Silvia Zuffi, Angjoo Kanazawa, Tanya Berger-Wolf, and Michael Black. Three-d safari: Learning to estimate zebra pose, shape, and texture from images “in the wild”. In *ICCV*, 2019. 2
- [72] Silvia Zuffi, Angjoo Kanazawa, and Michael J. Black. Lions and tigers and bears: Capturing non-rigid, 3D, articulated shape from images. In *CVPR*, 2018. 2
- [73] Silvia Zuffi, Angjoo Kanazawa, David Jacobs, and Michael J. Black. 3D menagerie: Modeling the 3D shape and pose of animals. In *CVPR*, 2017. 2